# Electron beam irradiation of dimethyl-(acetylacetonate) gold(III) adsorbed onto solid substrates

Joshua D. Wnuk,[1] Justin M. Gorham,[1] Samantha G. Rosenberg,[1] Willem F. van Dorp,[2,3] Theodore E. Madey,[2,a)] Cornelis W. Hagen,[3] and D. Howard Fairbrother[1,b)]
[1]*Department of Chemistry, Johns Hopkins University, Baltimore, Maryland 21218, USA*
[2]*Department of Physics and Astronomy and Laboratory for Surface Modification, Rutgers, The State University of New Jersey, Piscataway, New Jersey 08854-8019, USA*
[3]*Faculty of Applied Sciences, Delft University of Technology, Lorentzweg 1, 2628CJ Delft, The Netherlands*

(Received 2 October 2009; accepted 29 December 2009; published online 1 March 2010)

Electron beam induced deposition of organometallic precursors has emerged as an effective and versatile method for creating two-dimensional and three-dimensional metal-containing nanostructures. However, to improve the properties and optimize the chemical composition of nanostructures deposited in this way, the electron stimulated decomposition of the organometallic precursors must be better understood. To address this issue, we have employed an ultrahigh vacuum-surface science approach to study the electron induced reactions of dimethyl-(acetylacetonate) gold(III) [$Au^{III}(acac)Me_2$] adsorbed onto solid substrates. Using thin molecular films adsorbed onto cooled substrates, surface reactions, reaction kinetics, and gas phase products were studied in the incident energy regime between 40 and 1500 eV using a combination of x-ray photoelectron spectroscopy (XPS), reflection absorption infrared spectroscopy (RAIRS), and mass spectrometry (MS). XPS and RAIRS data indicate that electron irradiation of $Au^{III}(acac)Me_2$ is accompanied by the reduction in $Au^{III}$ to a metallic $Au^0$ species embedded in a dehydrogenated carbon matrix, while MS reveals the concomitant evolution of methane, ethane, carbon monoxide, and hydrogen. The electron stimulated decomposition of $Au^{III}(acac)Me_2$ is first-order with respect to the surface coverage of the organometallic precursor, and exhibits a rate constant that is proportional to the electron flux. At an incident electron energy of 520 eV, the total reaction cross section was $\approx 3.6 \times 10^{-16}$ $cm^2$. As a function of the incident electron energy, the maximum deposition yield was observed at $\approx$175 eV. The structure of discrete Au-containing deposits formed at room temperature by rastering an electron beam across a highly ordered pyrolytic graphite substrate in the presence of a constant partial pressure of $Au^{III}(acac)Me_2$ was also investigated by atomic force microscopy. © *2010 American Institute of Physics*. [doi:10.1063/1.3295918]

## I. INTRODUCTION

Electron beam lithography (EBL) is a well established nanofabrication technology, capable of defining a deposition pattern via the destruction of a resist layer with a focused electron beam; the current resolution for this technology is approximately 8 nm.[1] However, smaller scaled, single nanometer sized objects can be deposited using focused electron beam irradiation of a substrate under vacuum conditions in the presence of a partial pressure of suitable precursor molecules.[2,3] In addition to the ability to deposit smaller nanosized features compared to EBL, a distinct advantage of this direct-write process, referred to as focused electron beam induced processing (FEBIP), is its ability to deposit complex, two-dimensional and three-dimensional structures in one step. Examples of materials deposited with FEBIP are metals such as gold, platinum, tungsten, copper, iron, rhodium, and nickel, as well as nonmetals such as carbon, carbon nitride, and silicon dioxide.[4–14] FEBIP deposited structures have potential medicinal, industrial, and research applications as sensors, catalysts, nanowires, nanoelectronic components, and as high aspect ratio scanning probe tips.[8,15–24]

Typical FEBIP precursors used to deposit metallic nanostructures are organometallic molecules possessing carbonyl or alkyl ligands, which are chosen on the basis of their relatively high vapor pressures at room temperature. Examples of organometallic FEBIP precursors include tungsten hexacarbonyl, hexafluoracetylacetonate Cu(I) vinyltrimethylsilane, and trimethyl-(methylcyclopentadienyl) platinum(IV). In many organometallic gold precursors, a common component is the bidentate ligand acetylacetonate (acac), including dimethyl-(acetylacetonate) gold(III) [$Au^{III}(acac)Me_2$], dimethyl-(hexafluoroacetylacetonate) gold(III) [$Au^{III}(hfac)Me_2$], and dimethyl-(trifuoroacetylacetonate) gold(III) [$Au^{III}(tfac)Me_2$].[3,15,17,18,20,25–30] For example, using $Au^{III}(acac)Me_2$, plasmonic gold nanostructures with potential optical applications have been deposited using FEBIP; the same precursor has also been used to solder carbon nanotubes to gold electrodes. $Au^{III}(tfac)Me_2$ has been used in

a)Deceased.
b)Author to whom correspondence should be addressed. Electronic mail: howardf@jhu.edu.

 

FEBIP to deposit field emitter tips and a freestanding, circular wire extractor for potential use as a field emission source.[18,26,30]

At a molecular level, FEBIP occurs as a consequence of primary, secondary, or backscattered electrons interacting with transiently adsorbed precursor molecules, resulting in the electron stimulated decomposition of the precursor and the formation of nonvolatile products that serve as the building blocks for the growth of nanostructures.[31] However, metal-containing nanostructures deposited from organometallic precursors often contain high levels of organic contamination, associated with atoms (predominantly carbon) that were originally part of the ligand architecture.[5,18,32–36] As a result, FEBIP nanostructures often possess material characteristics that render them unsuitable for many electronic and optical applications (e.g., high resistivity). In contrast, purely inorganic precursors, that lack any carbon atoms, have been shown to form deposits with comparatively higher metal content than organometallic precursors (those that contain carbon). As a result, nanowires deposited from $AuClPF_3$ have been shown to possess an electrical conductance three orders of magnitude greater than those deposited from organometallic precursors.[35] However, $AuClPF_3$, like many inorganic precursors, is extremely unstable, being light sensitive and decomposing upon contact with metal surfaces, rendering it practically inappropriate for FEBIP applications. Another approach to improve the materials properties of FEBIP nanostructures is to use different ligand architectures in the organometallic precursor. However, as a necessary step toward the development of rational design criteria for organometallic precursors that can produce FEBIP deposits with lower levels of contamination and thus improved materials properties, more detailed molecular level information on the electron stimulated dissociation of existing organometallic precursors adsorbed onto solid substrates is required.

To date, most FEBIP studies have focused on obtaining structural information on deposited structures (i.e., volume, height, and composition) using techniques such as transmission electron microscopy and energy dispersive x-ray spectroscopy, as well as their corresponding materials properties (i.e., conductivity and tensile strength).[37] While this approach provides important information on the influence that experimental parameters have on the properties of FEBIP nanostructures, these studies cannot be used to extract mechanistic details on the deposition process.[38] To overcome this obstacle, an experimental approach must be adopted that allows the effect of electron irradiation on molecularly adsorbed precursors to be followed *in situ* and in real time. The present investigation demonstrates how such mechanistic information can be obtained by using surface analytical techniques to study the effect of electron irradiation on organometallic precursors condensed onto solid substrates at low temperatures under ultrahigh vacuum (UHV) conditions.[39] In part, this experimental approach is facilitated by the fact that nonadiabatic processes, such as the electron stimulated process involved in FEBIP, will be temperature independent. Under the low temperature UHV conditions prevalent in the present investigation, x-ray photoelectron spectroscopy (XPS) can inform on electron induced changes in the elemental composition of the adsorbate layer and oxidation state of metal atoms. Complementary information can also be obtained from infrared (IR) spectroscopy, which is capable of observing changes in the molecular bonding within adsorbed precursors, including the formation of any irradiation induced intermediates. Furthermore, by performing these studies under UHV conditions, gas phase products evolved during electron irradiation of the precursor can be analyzed by mass spectrometry (MS).

One intrinsic limitation of surface analytical techniques such as XPS and IR is that they require an analysis area ($>mm^2$) significantly larger than that of typical FEBIP deposits ($<100\ nm^2$). To overcome this limitation, reactions must be initiated over a larger surface area. Toward this end, we have shifted the paradigm from that of three-dimensional, nanosized objects to a two-dimensional thin film adsorbed onto a substrate with a macroscopic surface area ($\approx 1\ cm^2$). Specifically, in this study, we have considered the effect of electron irradiation on nanometer scale thick condensed films of the FEBIP gold precursor, $Au^{III}(acac)Me_2$. Throughout our studies, we have used comparatively low energy incident electrons ($<2$ keV). This decision was mitigated by the availability of broad beam electron sources in the low energy regime and the fact that reaction cross sections of adsorbed organometallics have been observed to exhibit maximum values at incident electron energies below 500 eV, significantly lower than the incident electron energies used in typical FEBIP experiments ($>5$ keV).[36,40] To complement our molecular level UHV studies, a limited number of experiments were also performed to investigate the structure of materials deposited when a substrate was electron irradiated at room temperature in the presence of a partial pressure of $Au^{III}(acac)Me_2$; conditions more representative of those encountered during FEBIP.

## II. EXPERIMENTAL METHODS

The majority of electron beam induced deposition experiments were performed under UHV conditions on molecularly adsorbed films of $Au^{III}(acac)Me_2$ deposited at low temperature ($\approx 160$ K) and exposed to broad beam electron irradiation. In these low temperature studies, the surface reactions and reaction kinetics of the electron induced deposition were probed *in situ* and in real time by XPS, reflection absorption IR spectroscopy (RAIRS), and MS.[39,41,42] These studies were augmented by a more limited set of experiments performed at room temperature to investigate the surface microstructure of structures resulting from the use of a more focused electron beam (spot size $\approx 1.5\ \mu m$) in the presence of a constant partial pressure of $Au^{III}(acac)Me_2$; these room temperature deposited films were studied *ex situ* using atomic force microscopy (AFM).

### A. Adsorbate

Dimethyl-(acetylacetonate) gold(III) (Strem Chemicals), $Au^{III}(acac)Me_2$, is a volatile, crystalline solid which sublimes at $\approx 25\ ^\circ C$. The structure of $Au^{III}(acac)Me_2$, a square-planar, $d^8$ organometallic complex, is shown in Fig. 1. Prior to dos-

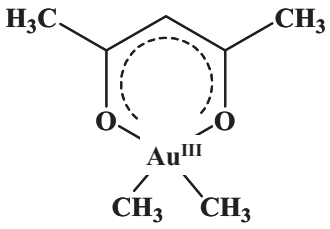


FIG. 1. The molecular structure of dimethyl-(acetylacetonate) gold(III), $Au^{III}(acac)Me_2$ [$CH_3COCHCOCH_3Au(CH_3)_2$].

ing into the UHV chamber, the $Au^{III}(acac)Me_2$ was stored in a glass finger that was attached to a gas manifold via a glass-to-metal seal.

### B. Molecular level studies using condensed nanoscale thin films of $Au^{III}(acac)Me_2$

Electron beam induced deposition studies were performed in two UHV chambers, one equipped with capabilities for XPS and MS, and the other with the capabilities for RAIRS. In both chambers, substrates were mounted at the end of manipulator arms with capabilities for *XYZ* translation and 360° rotation. A type K thermocouple, adhered to the underside of the sample holders, was used to measure temperature.

#### 1. Substrates

Three different substrates were used; for XPS experiments, a polycrystalline Ag foil and an amorphous carbon (a:C) substrate were used. The a:C substrate was generated by sputtering a 1.6 $cm^2$ highly ordered pyrolytic graphite (HOPG) substrate (SPI Supplies) with >2 keV $Ar^+$ (>1 h). The a:C substrate was chosen as a surrogate for a surface on which FEBIP experiments are typically performed. However, the a:C substrate does not allow XPS to determine (i) the fate of the carbon atoms present in the $Au^{III}(acac)Me_2$ precursor, (ii) film thickness, or (iii) changes in the stoichiometry of the film as a result of electron irradiation. To overcome these obstacles, comparative XPS experiments were performed using a Ag substrate. The polycrystalline Ag foil (Aldrich, 1.5 $cm^2$) was used as received and cleaned between experiments by sputtering the surface with 4 keV $Ar^+$ ions. The use of both Ag and a:C substrates also allowed us to observe any substrate effects, in terms of electron induced reaction kinetics or reaction products. For MS experiments, a polycrystalline Au substrate was used; for RAIRS experiments a Au (5.7 $cm^2$) mirror was used to enhance IR reflectivity.

#### 2. Film deposition

To create molecular thin films of $Au^{III}(acac)Me_2$, the precursor was dosed into the UHV chambers at a pressure of $\approx 2\times10^{-7}$ Torr; the gas purity was confirmed by MS. In the XPS/MS chamber, $Au^{III}(acac)Me_2$ was directionally dosed onto the substrate through a stainless steel tube. In the RAIRS chamber, the precursor was adsorbed by backfilling the chamber. During dosing, substrate temperatures of ≈160 K facilitated $Au^{III}(acac)Me_2$ adsorption and prevented unwanted coadsorption of water.[43] Low molecular weight species, such as $H_2O$, present in the vacuum chamber were either adsorbed onto the cooled manipulator arm (T <120 K) or pumped away; the base pressure after precursor dosing was routinely $<8\times10^{-10}$ Torr. During electron irradiation, surface temperatures were maintained at ≈160 K (XPS and MS chamber) and 100–160 K (RAIRS chamber).

#### 3. Determination of film thickness

In XPS experiments, the thickness of the $Au^{III}(acac)Me_2$ adsorbate layer was determined by measuring the attenuation of the substrate Ag (3*d*) signal using Eq. (1),

$$\text{Film thickness} = -\left[\lambda_{\text{Ag}(3d)}\cos(\theta)\ln\left(\frac{\text{Ag}}{\text{Ag}_0}\right)\right], \quad (1)$$

where $\lambda_{Ag(3d)}$ represents the inelastic mean free path of the Ag (3*d*) photoelectrons (1.32 nm), $\theta$ is the photoelectron take off angle with respect to the surface normal (54°), and Ag and $Ag_0$ are the Ag (3*d*) XPS peak areas after and before film deposition, respectively.[44] For experiments performed on the Ag substrate, the film thicknesses reported in this study were $1.0\pm0.3$ nm unless otherwise noted. Comparable film thicknesses of $Au^{III}(acac)Me_2$ were deposited onto the a:C substrate by controlling the deposition conditions so that the integrated area of the Au (4*f*) spectral envelope resulting from adsorbed $Au^{III}(acac)Me_2$ was similar to the Au (4*f*) XP areas obtained for ≈1.0 nm films deposited on Ag substrates. A comparison between the measured film thicknesses used in this study and the molecular diameter of $Au^{III}(acac)Me_2$ (1.5 nm average molecular diameter) suggests ≈1 ML average coverage.[45] In MS experiments, film thicknesses were similarly determined by measuring the attenuation of the Au (4*f*) peaks. In RAIRS measurements, film thicknesses were not quantitatively determined but are estimated to be <10 nm.

#### 4. Surface and gas phase analysis

XPS (Physical Electronics 5400 system) was performed using a magnesium coated x-ray source (Mg $K\alpha$, 1253.6 eV) operating at 15 kV and 300 W. Ejected photoelectrons were analyzed by a multichannel hemispherical analyzer and XP spectra were deconvoluted using commercially available software. All peak positions have been aligned to the $C-C/CH_2$ peak at 284.5 eV.[46] Based on the Au (4*f*) spectral envelope obtained for adsorbed $Au^{III}(acac)Me_2$, all Au ($4f_{5/2}/4f_{7/2}$) transitions were fit using 60% Gaussian/40% Lorentzian peaks and a spin-orbit splitting of 3.67 eV. Throughout the rest of the text, different gold species will be described in terms of their Au ($4f_{7/2}$) peak position.

Prolonged x-ray exposure produced changes in the Au (4*f*) region of adsorbed $Au^{III}(acac)Me_2$ molecules, analogous to the effects of electron induced reduction.[47] However, after 20 min of x-ray exposure, no observable reduction in the $Au^{III}$ species had occurred on the a:C substrate and less than a 4% reduction on Ag; though further irradiation resulted in greater decomposition on both substrates. Based on these results, each film was exposed to x-ray irradiation only twice, once before and once after electron exposure to cir-

cumvent the sensitivity of adsorbed $Au^{III}(acac)Me_2$ to x-ray irradiation. In this way each film was exposed to $<20$ min of total x-ray exposure. Consequently, changes in XPS spectra can be attributed solely to the effects of electron irradiation.

RAIRS spectra were recorded using a Mattson Infinity Series Fourier Transform IR spectrometer with a narrow band InSb detector ($1900-4000\ cm^{-1}$), operating at a resolution of $4\ cm^{-1}$. Neutral, gas phase products evolved during electron irradiation of adsorbed $Au^{III}(acac)Me_2$ molecules were detected using a quadrupole MS (Stanford Research Systems, 0–200 amu) positioned at a distance of ≈12 cm from the substrate and in a direct line of sight. In MS experiments, the filament was outgassed for several days to decrease the gas phase signal of volatile species produced from the heated filament to a level that was significantly smaller than the signal from gas phase species produced during electron irradiation of adsorbed $Au^{III}(acac)Me_2$.

#### 5. Electron source

A commercial flood gun (Specs 15/40) was used as the source of broad beam electron irradiation. The electron source was positioned perpendicular to the substrate with a sample-source distance of ≈12 cm in XPS/MS experiments and ≈32 cm in RAIRS experiments. The electron beam profile was characterized in the XPS/MS chamber using a Faraday cup attached to the end of the manipulator arm. Analysis of the beam profile showed that the beam profile was essentially independent of electron energy. Furthermore, by positioning the sample at the center of the beam and at a source to sample distance $>7$ cm, the electron flux across the surface was relatively uniform (≈10% change in flux across a 2.0 $cm^2$ substrate[47]). In each experiment, the incident electron energy was calculated from the sum of the electron energy generated by the flood gun and a positive bias (typically +20 V) applied to the substrate. This positive bias was necessary to ensure that the vast majority of the secondary electrons generated by the primary beam were recaptured by the substrate enabling a correct measure of the target current. The target current was measured to ground via a picoammeter (Keithley 1685) placed in series with the voltage source. The electron irradiation was measured in terms of the electron dose $d$ using Eq. (2),

$$d = \frac{I \times t}{A}, \tag{2}$$

where $I$ is the measured target current (electrons $s^{-1}$), $t$ is the duration of electron exposure (seconds), and $A$ is the sample area ($cm^2$). The power density of the incident electron beam, at an incident energy of 520 eV, in these low temperature, adsorbed molecular film studies was $\approx 2 \times 10^{-4}\ \mu W/\mu m^2$.

### C. Films deposited at room temperature in a partial pressure of $Au^{III}(acac)Me_2$

Electron beam induced deposition of transiently adsorbed $Au^{III}(acac)Me_2$ molecules was performed using the electron source of an Auger electron spectrometer (AES) (Physical Electronics 610; $LaB_6$ filament). For each experiment, deposition was performed on a freshly cleaved HOPG substrate. Fabrication of the electron beam deposited structure was accomplished by rastering the Auger electron beam (1.5 keV; ≈1.5 μm spot size) over the HOPG surface for 20 min in the presence of a reasonably constant partial pressure ($5.0 \times 10^{-8} - 1.5 \times 10^{-7}$ Torr) of $Au^{III}(acac)Me_2$ molecules. In these experiments, the substrate was at room temperature throughout the deposition process. The power density of the incident electron beam in these room temperature studies was $\approx 2 \times 10^2\ \mu W/\mu m^2$.

#### 1. Film characterization

The film's average chemical composition in these experiments was quantified by AES. The location and shape of films deposited by electron irradiation were monitored using the system's secondary electron detector (SED), while morphological analysis of selected films was performed *ex situ* under ambient conditions using AFM. The HOPG substrate onto which a film had been electron beam deposited was removed from the vacuum chamber and adhered to the AFM sample plate using double-sided carbon tape. SED images of the electron beam deposited structures in close proximity to physical markers (scribed into the HOPG substrate prior to deposition) were used in conjunction with an optical microscope attached to the AFM to locate the deposit. AFM images were acquired using a PicoSPM LE (Agilent Technologies) operating in magnetic tapping mode using magnetically coated probes (Micromasch NSC18 Co/Cr) operating at an oscillating frequency of ≈80 kHz. All image rendering and height measurements were performed using commercially available software from Agilent Technologies.

## III. RESULTS (UNLESS NOTED, ALL EXPERIMENTS WERE PERFORMED WITH 520 EV ELECTRONS)

### A. Surface chemistry

The XP spectra in Fig. 2 shows the effect of increasing electron irradiation on the Au (4*f*), C (1*s*), and O (1*s*) regions of a $Au^{III}(acac)Me_2$ film adsorbed at ≈160 K onto a Ag substrate. The right hand spectra in Fig. 2 shows the evolution in the Au (4*f*) region. Prior to electron irradiation (dose=0 $e^-\ cm^{-2}$), the Au (4*f*) spectral envelope can be well fit by one set of Au ($4f_{5/2}, 4f_{7/2}$) peaks with a Au ($4f_{7/2}$) peak at $86.2 \pm 0.3$ eV. This peak position is consistent with the binding energy expected for $Au^{III}$ atoms in the parent $Au^{III}(acac)Me_2$ molecule.[48] With the onset of electron irradiation, Fig. 2 shows that the Au (4*f*) spectral envelope broadens to lower binding energies. This Au (4*f*) spectral envelope can be well fit by a linear combination of two sets of Au ($4f_{5/2}, 4f_{7/2}$) peaks with Au ($4f_{7/2}$) peaks at ≈86.2 and 84.0 eV. The Au ($4f_{7/2}$) peak at ≈86.2 eV is associated with the parent $Au^{III}(acac)Me_2$ compound, while the Au ($4f_{7/2}$) peak at $84.0 \pm 0.2$ eV is ascribed to reduced Au atoms formed by electron reduction in adsorbed $Au^{III}(acac)Me_2$ species. The Au ($4f_{7/2}$) peak position at 84.0 eV that appears as a result of electron irradiation is virtually identical to that of metallic gold ($Au^0$) sputter deposited onto Ag; shown as the top right hand spectrum of Fig. 2. It should be noted that the spectral envelope associated with this reduced Au species

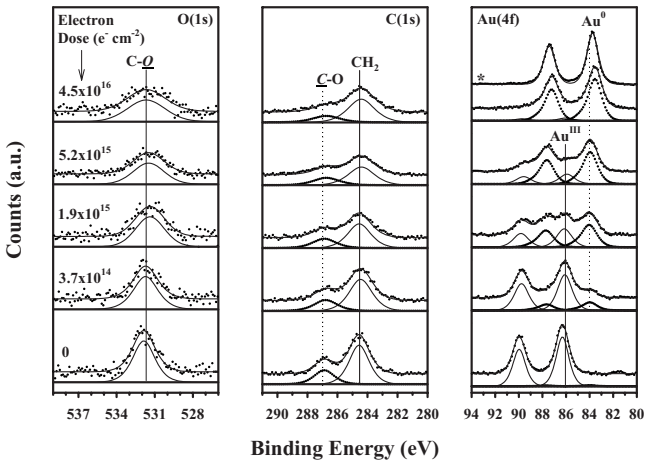


FIG. 2. Evolution of the O (1*s*), C (1*s*), and Au (4*f*) regions during electron irradiation of $Au^{III}(acac)Me_2$ adsorbed onto a silver substrate at ≈160 K. Irradiation was performed at an incident electron energy of 520 eV and a flux of ≈2.0 $\mu$A cm$^{-2}$. To compensate for the slight variations in initial film thicknesses between different experiments, the XPS spectra have all been normalized to the area of the Au (4*f*) region measured prior to electron irradiation. The asterisk in the top right spectrum denotes the Au (4*f*) spectrum of gold sputter deposited onto silver.

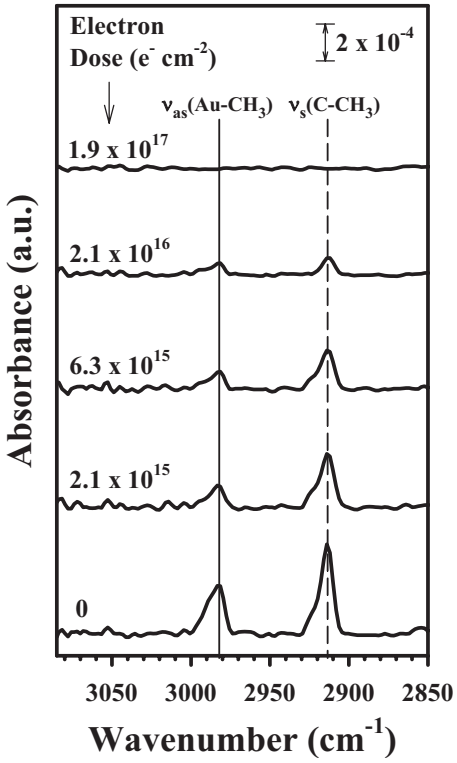


FIG. 3. Changes in the C–H stretching region of adsorbed $Au^{III}(acac)Me_2$ shown as a function of increasing electron dose. The dominant stretching modes, $\nu_s(CH_3)$ of the acac ligand (dashed) and $\nu_{as}(CH_3)$ of the methyl ligands (solid), are labeled for clarity. During irradiation, the electron energy was 520 eV and the flux was ≈11 $\mu$A cm$^{-2}$.

formed by electron beam irradiation, hereafter referred to as $Au^0$, exhibits a slight asymmetry toward higher binding energy compared to sputter deposited metallic gold. This asymmetry, which was observed on both a:C and Ag substrates, has been included in the deconvolution of the Au (4*f*) spectral envelope into the parent $Au^{III}$ atoms and the reduced $Au^0$ species. It should be noted that the initial Au ($4f_{7/2}$) peak of the $Au^{III}(acac)Me_2$ consistently shifts ≈0.2 eV to lower binding energy immediately after the onset of electron irradiation, a phenomenon that has been observed previously in related studies of other organometallic precursors.[39] It should be noted that this shift is not associated with the formation of any intermediate species as evidenced by a lack of change in the IR spectra (see Fig. 3).

Figure 2 shows that the Au (4*f*) spectral envelope continues to evolve as a function of increasing electron dose. Deconvolution of the Au (4*f*) region reveals that the spectral intensity of the parent $Au^{III}$ species decreases to 46% of its initial value after an electron dose of $1.9\times10^{15}$ e$^-$ cm$^{-2}$ and to 24% after an electron dose of $5.2\times10^{15}$ e$^-$ cm$^{-2}$, while there is a corresponding increase in the coverage of $Au^0$ species. Indeed, for an electron dose of $4.5\times10^{16}$ e$^-$ cm$^{-2}$, reduction of the parent $Au^{III}$ species is essentially complete, and longer irradiation times did not produce any additional changes in the Au (4*f*) region. It should be noted that despite changes in the shape of the Au (4*f*) spectral envelope there was <5% change in the total integrated intensity in the Au (4*f*) region as a result of electron exposure.

Prior to electron irradiation, the C (1*s*) region of the molecularly adsorbed $Au^{III}(acac)Me_2$ precursor has two well defined spectral features at ≈284.5 eV ($C-C/CH_2$) and at ≈287.0 eV, the latter originating from the C–O bonds in the acac ligand.[49] After an electron dose of $4.5\times10^{16}$ e$^-$ cm$^{-2}$, the most visible change in the C (1*s*) region is a broadening of both spectral features from a full width at half maximum (FWHM) of 1.6 to 2.1 eV. After electron irradiation there is, however, a slight reduction (≈15%) in the integrated area of the C (1*s*) region and a reduction in the $\underline{C}-O:\underline{C}H_2$ ratio. The O (1*s*) region initially exhibits a single spectral feature at ≈532 eV, a value which is characteristic of the $\underline{O}-C$ bonding in the acac ligand.[49,50] After an electron dose of $4.5\times10^{16}$ e$^-$ cm$^{-2}$, there is a 60% decrease in the area in the O (1*s*) peak area and a concomitant increase in the FWHM from 2.0 to 3.5 eV.

For experiments performed on Ag substrates, quantitative changes in the film's stoichiometry and film thickness as a result of electron irradiation could also be determined. On the basis of ten separate experiments it was determined that the Au:C:O stoichiometry changes from 1:7:2 to 1:6:0.8 as a result of the electron induced decomposition of adsorbed $Au^{III}(acac)Me_2$. In addition to changes in the film's average stoichiometry, a consistent decrease in the film's average thickness was observed from $1.0\pm0.3$ to $0.8\pm0.3$ nm after prolonged electron irradiation.

The RAIRS spectra in Fig. 3 highlight the changes in the C–H bonding of a $Au^{III}(acac)Me_2$ film, specifically the dominant stretching modes at 2915 cm$^{-1}$ [$\nu_s(CH_3)$ of the acac ligand] and 2985 cm$^{-1}$ [$\nu_{as}(CH_3)$ of the Au-methyl ligands], as a function of increasing electron dose.[51] Each IR spectrum has been ratioed to the spectrum of the film obtained after a prolonged electron dose of $2.8\times10^{17}$ e$^-$ cm$^{-2}$; a situation that resulted in a featureless background that remained invariant to further electron irradiation. Analysis of Fig. 3 reveals that both the $\nu_s(CH_3)$ and $\nu_{as}(CH_3)$ modes lose intensity at comparable rates during electron irradiation and over

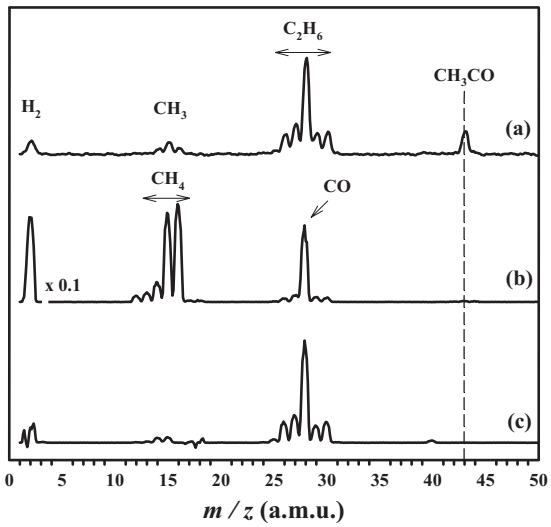


FIG. 4. Mass spectrum (0–50 amu; background corrected) obtained from the electron irradiation of $Au^{III}(acac)Me_2$ (a) in the gas phase and (b) adsorbed onto a gold substrate at ≈100 K. Reference mass spectra for ethane is shown in (c). The gas phase products in (b) were recorded during the initial period (0–20 s) of electron irradiation, at an incident energy of 500 eV and a flux of ≈25 $\mu$A cm$^{-2}$. In (b), the low $m/z$ region (<5) has been reduced to 10% of its original intensity to scale the hydrogen signal at $m/z=2$. In (a) the background spectra was recorded at a chamber pressure of ≈2 $\times 10^{-9}$ Torr. In (b), the mass spectrum of the clean gold substrate irradiated by electrons at the same energy and flux was used as the background.

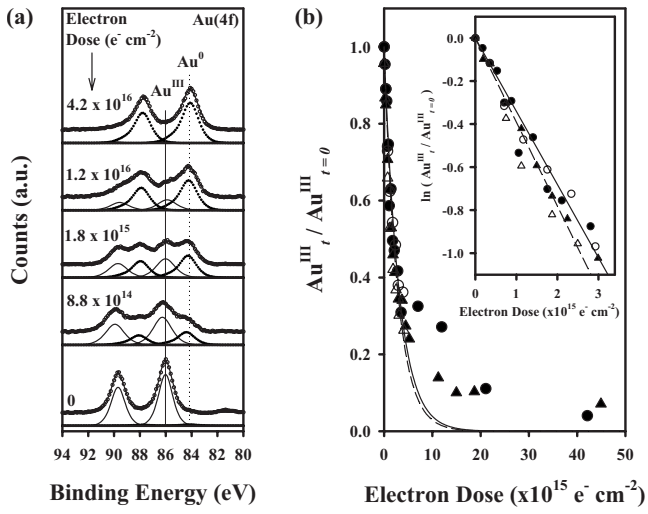


FIG. 5. (a) Changes in the Au ($4f$) XP region of $Au^{III}(acac)Me_2$ adsorbed onto a:C, measured as a function of increasing electron dose at a constant incident electron energy of 520 eV. The solid line denotes the Au ($4f_{7/2}$) peak position of the parent $Au^{III}$ species, and the dotted line that of the $Au^0$ irradiation product. (b) The loss in $Au^{III}$ spectral intensity (normalized to the $Au^{III}$ signal measured prior to electron irradiation) is plotted as a function of the electron dose. The inset in (b) shows the initial loss of $Au^{III}$ plotted on a log scale where the best-fit lines are shown for a first-order decay process. In (a) and (b), data from $Au^{III}(acac)Me_2$ molecules adsorbed onto both a:C (circles) and Ag (triangles) substrates are shown; filled symbols represent data obtained when the incident electron flux was held constant while the exposure time was varied, while open symbols are from studies where the irradiation time was held constant and the electron flux varied. Solid lines denote experiments conducted on a:C and dashed lines for those conducted on silver.

a timescale comparable to the one observed by XPS in Fig. 2 for the reduction in $Au^{III}$ to $Au^0$ species. Figure 3 also shows that the loss of vibrational intensity associated with the methyl groups in the parent compound is not accompanied by the appearance of any vibrational bands within the C–H stretching region associated with product species.

Figures 4(a) and 4(b) show a comparison of the neutral gas phase species produced during electron irradiation of (a) *gas phase* and (b) *adsorbed* $Au^{III}(acac)Me_2$ molecules. Figure 4(a) shows the fragmentation pattern observed from $\approx 1.0 \times 10^{-6}$ Torr, gas phase $Au^{III}(acac)Me_2$. The MS is dominated by a peak at $m/z=43$ and peaks between $m/z=26$ and 30. The peak at $m/z=43$ can be identified as $CH_3CO$, the largest fragment associated with the acac ligand.[52,53] The fragmentation pattern between $m/z=26$ and 30 is consistent with the reference spectra of ethane (Specialty Gases of America, Inc.), shown in Fig. 4(c). Smaller peaks at $m/z=2$ and $m/z=15$ in Fig. 4(a) can be ascribed to diatomic hydrogen and methyl radicals formed during electron stimulated decomposition of gas phase $Au^{III}(acac)Me_2$, respectively.

Figure 4(b) illustrates the volatile species produced when a ≈2.3-nm-thick $Au^{III}(acac)Me_2$ film, adsorbed onto Au, is exposed to electron irradiation (flux=25 $\mu$A cm$^{-2}$). Analysis of Fig. 4(b) reveals the presence of an intense hydrogen ($m/z=2$) peak and spectral intensity between $m/z=12$ and 16, the latter consistent with the production of methane. Additional fragments are observed between $m/z=26$ and 30, with a prominent peak at $m/z=28$. The intensity variation in the fragments between $m/z=26$ and 30 can be accounted for by the production of ethane [see Fig. 4(c)] and an additional fragment with intensity at $m/z=28$. Based on the structure of $Au^{III}(acac)Me_2$ we believe that this additional intensity at $m/z=28$ is a result of carbon monoxide (CO) being evolved during electron irradiation. Figure 4(b) also shows that there is no evidence of any spectral intensity at $m/z=43$ ($CH_3CO$), implying an absence of electron stimulated desorption of the parent compound. It should also be noted that the production of the various gas phase species ($CH_4$, $C_2H_6$, CO, and $H_2$) occurred over a timescale comparable to that of the $Au^{III}$ reduction observed by XPS (Fig. 2), although the intensity of the MS signals did not permit a detailed time-resolved study to be performed.

### B. Electron stimulated reaction kinetics

In Fig. 5, the electron stimulated reduction kinetics of surface adsorbed $Au^{III}(acac)Me_2$ species are considered explicitly. Figure 5(a) illustrates the effect of varying electron exposure time (0, 75, 150, 1020, and 3600 s) on the Au ($4f$) region of adsorbed $Au^{III}(acac)Me_2$ molecules adsorbed onto an a:C substrate for a fixed electron flux (≈1.9 $\mu$A cm$^{-2}$). As the irradiation time increases there is a smooth and systematic broadening of the Au ($4f$) spectral envelope to lower binding energies. This occurs as a result of the electron induced reduction in parent $Au^{III}$ species [Au ($4f_{7/2}$) position $86.1 \pm 0.1$ eV] to the $Au^0$ product [Au ($4f_{7/2}$) peak position=$84.3 \pm 0.1$ eV], analogous to the behavior observed in Fig. 2 for $Au^{III}(acac)Me_2$ molecules adsorbed onto a Ag substrate. Deconvolution of the Au ($4f$) spectra in Fig. 5(a) shows that increasing the electron dose results in films that possess 75% ($8.8 \times 10^{14}$ e$^-$ cm$^{-2}$), 50% (1.8

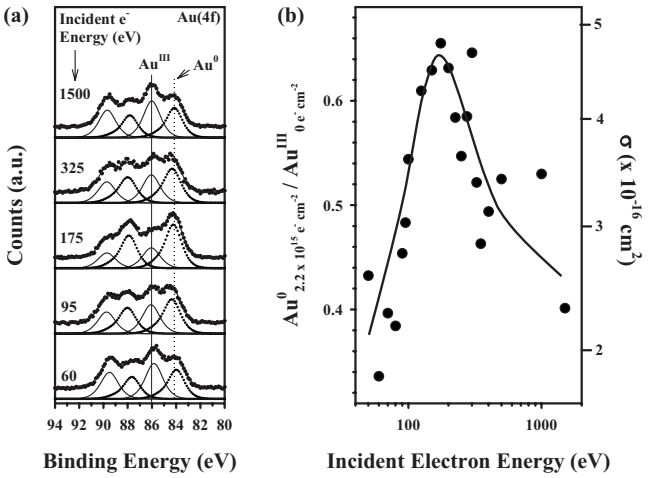


FIG. 6. The influence of incident electron energy on the extent of $Au^{III}$ reduction. (a) Change in the Au ($4f$) region for $Au^{III}(acac)Me_2$ molecules, adsorbed onto a:C ($\approx$160 K) and exposed to a consistent electron dose ($2.2\times10^{15}$ $e^-$ $cm^{-2}$), plotted as a function of the incident kinetic energy. The solid line in (a) denotes the position of the Au ($4f_{7/2}$) peak associated with the parent $Au^{III}$ species, while the dotted line represents that of the $Au^0$ product. (b) Extent of reaction after a fixed electron dose ($2.2\times10^{15}$ $e^-$ $cm^{-2}$), as measured by the fractional production of $Au^0$ atoms (left hand axis) and the corresponding reaction cross sections (right hand axis) assuming a first-order process, plotted as a function of the incident electron energy. The solid line through the experimental data is drawn merely as a guide to the eye.

$\times10^{15}$ $e^-$ $cm^{-2}$), 27% ($1.2\times10^{16}$ $e^-$ $cm^{-2}$), and <4% ($4.2\times10^{16}$ $e^-$ $cm^{-2}$) of the initial $Au^{III}(acac)Me_2$.

For molecular $Au^{III}(acac)Me_2$ films adsorbed onto either a:C (circles) or Ag (triangles) substrates, the fraction of $Au^{III}(acac)Me_2$ remaining has been plotted as a function of electron dose in Fig. 5(b). The electron dose can be varied either by adjusting the incident flux or the exposure time. Figure 5(b) shows data obtained from both methods, while the inset shows the initial electron stimulated loss kinetics of $Au^{III}(acac)Me_2$, plotted in terms of $\ln(Au^{III}{}_t/Au^{III}{}_{t=0})$. In Fig. 5(b), the solid and dashed lines are the best-fit results obtained from analyzing the data on the basis of a first-order decay process with respect to electron dose, for $Au^{III}(acac)Me_2$ molecules adsorbed onto a:C or Ag substrates, respectively.

The effect of incident electron energy on the efficiency of the $Au^{III}$ reduction process is illustrated in Fig. 6. In each of the Au ($4f$) spectral envelopes shown in Fig. 6(a), adsorbed $Au^{III}(acac)Me_2$ molecules on a:C ($\approx$160 K) have been exposed to the same electron dose ($2.2\times10^{15}$ $e^-$ $cm^{-2}$) but at different incident electron energies. Figure 6(a) illustrates that regardless of the incident electron energy, the Au ($4f$) region can be fit by a linear combination of spectral envelopes associated with the parent $Au^{III}$ species and the reduced $Au^0$ product. However, analysis of Fig. 6 also reveals that the extent of reaction varies as a function of incident electron energy. This is shown more explicitly in Fig. 6(b) where the fraction of $Au^0$ species produced after a constant electron dose ($2.2\times10^{15}$ $e^-$ $cm^{-2}$) has been plotted as a function of the incident electron energy. Figure 6(b) illustrates that the extent of reaction varies smoothly as a function of incident energy, with a maximum at $\approx$175 eV. The line in Fig. 6(b) is intended solely as a guide to the eye.

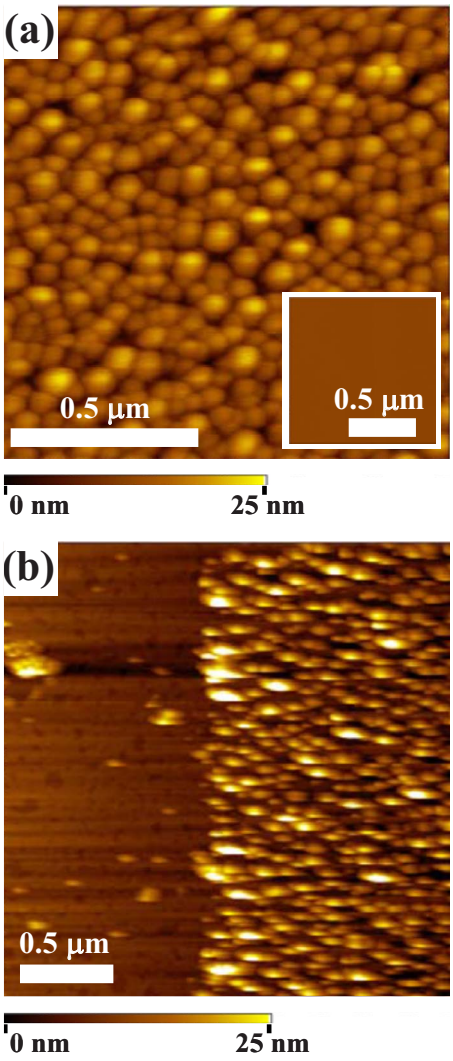


FIG. 7. (Color online) (a) Topographic AFM image of a film generated by the electron irradiation (beam diameter $\approx$1.5 $\mu$m, beam energy=1.5 keV) of HOPG at room temperature in the presence of a roughly constant partial pressure of $Au^{III}(acac)Me_2$ molecules ($5\times10^{-8}$–$1.5\times10^{-7}$ Torr). The inset shows an AFM image of the HOPG substrate obtained outside of the deposition area. (b) Topographic image revealing the contrast between the underlying substrate and the electron beam deposited film.

### C. Structure of deposited films

AFM was used to probe the microstructure of a film that was deposited by rastering an electron beam over a $\approx400\times500$ $\mu m^2$ region of a HOPG substrate in the presence of a constant partial pressure of $Au^{III}(acac)Me_2$. In Fig. 7(a), a topographic image of the deposited material has been juxtaposed with an image of the HOPG substrate obtained outside of the deposition area (both shown on the same height scale). The presence of gold atoms in the deposition region was verified using AES.[47] Thus, the discrete, spherical shaped objects in Fig. 7(a) can be identified as having originated from the electron irradiation of transiently adsorbed $Au^{III}(acac)Me_2$ molecules. To facilitate a direct comparison of the deposited film's topography with that of the underlying HOPG substrate, the AFM tip was used to remove de-

posited structures from a selected area by decreasing the tip's oscillatory amplitude, thereby increasing the force exerted by the tip on the film. Topographic [Fig. 7(b)] images of an area bisecting the deposited film and the exposed HOPG substrate accentuate the differences in the two regions. Analysis of the deposited structures yielded an average height of $15.6 \pm 4.5$ nm. It should be noted that tip dilation effects mean that only height measurements are quantitative.

## IV. DISCUSSION

The discussion is organized as follows: the influence of electron irradiation is first considered in terms of the surface reactions of adsorbed $Au^{III}(acac)Me_2$ and resultant changes in surface composition. Next, the electron stimulated reaction kinetics and reaction cross sections are discussed, followed by the role that the incident electron energy plays in determining the deposition rate. In Sec. IV D, the structure of films deposited under ambient conditions using a more focused electron beam is discussed. The significance and implications of results obtained in this investigation as they pertain to FEBIP processes are also considered.

### A. Electron stimulated surface reactions and products

Figures 2, 5, and 6 demonstrate that the reduced gold species $Au^0$ formed by electron irradiation of adsorbed $Au^{III}(acac)Me_2$ exhibits the same Au $(4f_{7/2})$ peak position as vapor deposited, metallic gold. Although the peak position of the reduced species is consistent with gold atoms in a metallic state, the Au $(4f)$ XPS peak profile displays a slight asymmetry to higher binding energy compared to the sputter deposited gold atoms [for example, see topmost spectra in Fig. 5(a)]. This increase in heterogeneity is probably a reflection of the fact that the gold atoms produced by the electron beam induced decomposition of $Au^{III}(acac)Me_2$ are embedded in an organic matrix, composed principally of carbon atoms.

In addition to the reduction in $Au^{III}$ species to $Au^0$, electron irradiation changes the chemical composition of the film. Based on XPS analysis of films formed after prolonged irradiation (sufficient to reduce all $Au^{III}$ species), electron irradiation leads to a loss of approximately one carbon atom and one oxygen atom for each parent $Au^{III}(acac)Me_2$ molecule that undergoes decomposition. Thus, the overall change in the film's composition that occurs as a result of electron irradiation can be represented by Eq. (3),

$$Au^{III}C_7O_{2(ads)} + e^- \rightarrow \rightarrow Au^0C_6O_{0.8(s)}. \quad (3)$$

The formation of a metal-containing organic matrix composed of Au, C, and O atoms is also believed to be responsible for the increase in FWHM of the O $(1s)$ and C $(1s)$ spectral envelopes as the heterogeneity in the local environment of these atoms will have increased compared to molecular $Au^{III}(acac)Me_2$. Furthermore, the chemical composition of the adlayer formed by electron irradiation does not change when the substrate is annealed from $\approx$160 K to room temperature. Thus, the majority of the carbon atoms within the precursor's ligand architecture become incorporated within the deposit formed during electron stimulated decomposition.

Concomitant with changes to the condensed phase, electron irradiation of adsorbed $Au^{III}(acac)Me_2$ molecules also leads to the evolution of methane, carbon monoxide, hydrogen, and ethane. These gas phase species are formed in the absence of any parent $Au^{III}(acac)Me_2$ desorption as evidenced by the lack of any spectral intensity at $m/z=43$ [Fig. 4(b)] and a $<5\%$ change in the integrated Au $(4f)$ XPS area (see Figs. 2, 5, and 6); carbon atoms lost from the adsorbate layer during electron irradiation are therefore released as either gas phase methane, ethane or carbon monoxide. In contrast, hydrogen atoms are removed from adsorbed $Au^{III}(acac)Me_2$ during electron irradiation predominantly in the form of molecular hydrogen, presumably as a result of electron stimulated C–H bond breaking processes. This assertion is consistent with the loss of all vibrational intensity associated with the C–H stretching modes of the parent compound (Fig. 3).

In summary, the known chemical reactions that accompany electron irradiation of adsorbed $Au^{III}(acac)Me_2$ can be expressed by Eq. (4).

$$Au^{III}(acac)Me_{2(ads)} + e^- \rightarrow \rightarrow Au^0C_6O_{0.8(s)} + H_{2(g)} + CH_{4(g)} + C_2H_{6(g)} + CO_{(g)}. \quad (4)$$

The formation of methane, ethane, and carbon monoxide also contributes to the decrease in average film thickness observed as a result of electron irradiation. However, it should be emphasized that despite the evolution of these gas phase species most of the carbon atoms present in the ligand architecture of the precursor become incorporated within the deposit. The similarity of the reactions observed on Ag, Au, and a:C suggests that the substrate does not influence the electron stimulated reaction products or surface chemistry.

A detailed analysis of the gas phase products evolved during electron irradiation can also provide mechanistic insights into the electron beam induced deposition process. For example, the evolution of CO requires cleavage of the Au–OC linkage; in this regard it should also be noted that the evolution of CO is also consistent with the loss of oxygen atoms from the adlayer observed by XPS as a result of electron irradiation [see Fig. 2 and Eq. (4)]. However, the presence of a measurable oxygen XPS signal in the fully irradiated film (see top spectra in Fig. 2) indicates that not all of the Au–OC linkages produce CO, and that some of the oxygen atoms initially associated with the acac ligand become incorporated into the organic matrix.

In previous studies, experiments performed on $MeCpPt^{IV}Me_3$ and $CpPt^{IV}Me_3$ provided strong support for the idea that in these Pt based organometallic precursor's methane formation was a consequence of electron stimulated $Pt-CH_3$ bond cleavage.[39] In an analogous fashion, we ascribe the methane observed in the present study to electron stimulated $Au-CH_3$ bond cleavage as opposed to $C-CH_3$ bond cleavage. This assertion is also supported by the fact that in recent studies on the electron beam induced deposition of $Ni^{II}(MeCp)_2$, which has only $C-CH_3$ bonds, hydrogen was the only volatile species detected. The small ethane signal observed during the electron irradiation of adsorbed

$Au^{III}(acac)Me_2$ is probably due to bimolecular coupling reactions between methyl radicals formed by $Au-CH_3$ bond cleavage.

It should be noted that for the proposed mechanisms for the formation of volatile carbon-containing species ($CH_4$, $C_2H_6$, and CO) that can escape the film during electron irradiation, both involve metal-ligand bond cleavage as opposed to reactions within the ligands themselves. It is this type of mechanistic insight that is needed to aid in the rationale design of precursors that will form FEBIP deposits with lower levels of organic contamination and thus exhibit more desirable materials properties. A comparison of Figs. 4(a) and 4(b) also highlights the fact that the state of the molecule (gas phase versus adsorbed) profoundly influences the nature of the volatile species produced during electron irradiation.

### B. Reaction kinetics

Kinetics have been obtained for the electron reduction in $Au^{III}(acac)Me_2$ using XPS (see Fig. 5). Based on the data shown in Fig. 5, the reduction in $Au^{III}$ species follows a first-order dependence with respect to electron dose ($d$) and can thus be described by Eq. (5),

$$[Au^{III}]_d = [Au^{III}]_{d=0} e^{-d\sigma} \quad [\sigma = \text{total reaction cross section } (cm^2)]. \quad (5)$$

It should be noted that the quality of the first-order fit observed on the basis of Eq. (5) is best for the initial period of the decay profile [see inset to Fig. 5(b)]. The poorer quality of the fit observed for prolonged irradiation times has been observed in previous XPS studies of electron reactions with FEBIP precursors.[39] Simulations based on data from Faraday cup measurements[47] revealed that the deviation of the decay profile shown in Fig. 5 from first-order kinetics could not be accounted for on the basis of the slight spatial heterogeneity in the electron flux across the surface.[54] The deviations from perfect adherence to first-order kinetics is probably a result of the analysis method, specifically the difficulty in accurately determining the contribution of the $Au^{III}$ signal to the Au ($4f$) spectral envelope when the $Au^{III}$ signal becomes comparatively small compared to the product $Au^0$ species (see, for example, the spectra in Fig. 5 at $1.2 \times 10^{16}$ $e^- cm^{-2}$). Another possibility is that as the reaction progresses, the reaction cross section for intact $Au^{III}(acac)Me_2$ molecules surrounded by $Au^0$ atoms embedded in a carbon matrix differs slightly from that of the $Au^{III}(acac)Me_2$ molecules in the purely molecular adlayer that exists at the onset of irradiation.[40]

Based on XPS data obtained on a:C and Ag substrates, the average total reaction cross-section values $\sigma$ on either substrate for an incident electron energy of 520 eV are reported in Table I.

Consistent with the similarity in surface reactions (see Sec. IV A of the discussion), Table I reveals that the total reaction cross section is largely independent of the substrate onto which the $Au^{III}(acac)Me_2$ molecules are adsorbed. Furthermore, since our experimental data indicate that the timescales for $Au^{III}$ reduction and the evolution of gas phase products are comparable for a given experiment, it appears that all of these various electron stimulated processes involve the same rate determining step and thus exhibit the same total reaction cross section. It should also be noted that the magnitude of the total reaction cross section determined for $Au^{III}(acac)Me_{2(ads)}$ is similar to measured values for $MeCpPt^{IV}Me_{3(ads)}$ at comparable incident electron energies ($2.2 \times 10^{16}$ $cm^2$ at 500 eV).[39,40]

TABLE I. Total reaction cross-section values measured for the electron stimulated decomposition of $Au^{III}(acac)Me_2$ adsorbed onto a:C and silver foil at an incident electron energy of 520 eV.

| | $\sigma_{ave,520\ eV}$ ($cm^2$) |
|---|---|
| a:C | $3.4 \pm 0.1 \times 10^{-16}$ |
| Ag | $3.9 \pm 0.4 \times 10^{-16}$ |

### C. Influence of the incident electron energy

In Fig. 6, the influence of the incident electron energy on the reaction efficiency, as measured by the total reaction cross section for $Au^{III}$ reduction for a fixed electron dose ($2.2 \times 10^{15}$ $e^- cm^{-2}$) assuming first-order kinetics, has been determined for incident electron energies in the range 40–1500 eV. The data plotted in Fig. 6(b) indicate that the maximum deposition yield occurs at an incident electron energy of ≈175 eV. Related experiments performed on the electron induced decomposition of the organometallic precursor $MeCpPt^{IV}Me_3$ have revealed that the decomposition efficiency and total reaction cross section also exhibit a similar functional dependence on the incident electron energy, with a maximum ≈150–200 eV.[40] From a practical standpoint, these results suggest that optimal growth rates in FEBIP will require incident electrons with energies close to 200 eV. However, there are a number of inherent difficulties in operating a focused electron beam below 1 keV. At a more molecular level, the decomposition of organometallic precursors such as $Au^{III}(acac)Me_2$ molecules on solid surfaces can in principle be initiated either by primary electrons or lower energy secondary/backscattered electrons generated by the interaction of the primary electron beam with the substrate. To determine the relative importance of secondary versus primary electrons, studies are required where both the yield and energy distribution of secondary/backscattered electrons can be determined in an experimental design that also allows for the simultaneous determination of reaction efficiency.

### D. Structure of electron beam deposits

Figure 7 clearly demonstrates that the gold-containing deposits formed by rastering an electron beam across a HOPG substrate do not exist as a uniform overlayer but are instead present as discrete, isolated structures. In this context, it should be noted that the diameter of the electron beam (≈1.5 $\mu$m spot size) is significantly larger than the size of the individually deposited spherical objects (<0.1 $\mu$m) and that even a crude AFM analysis indicates that each individual structure must have been formed from the electron stimulated decomposition of numerous precursor molecules. These

observations suggest that once the deposition process has been initiated, subsequent electron stimulated growth must occur preferentially on the gold-containing deposits rather than on the HOPG substrate. One possible explanation that would give rise to such a phenomenon is that the adsorption energy of $Au^{III}(acac)Me_2$ on gold-containing deposits is higher than that of $Au^{III}(acac)Me_2$ molecules on the HOPG substrate. Indeed, in a study of the electron beam induced deposition of $MeCpPt^{IV}Me_3$ onto gold, the sticking probability of FEBIP precursor molecules has been observed to increase on the electron beam deposited substrate as compared to the underlying substrate.[40] If the same phenomenon occurs under the experimental conditions relevant to Fig. 7, the steady-state concentration of transiently adsorbed $Au^{III}(acac)Me_2$ molecules on gold-containing deposits would be greater than on the HOPG substrate, leading to an effective nucleation phenomenon and the formation of discrete structures rather than a uniform overlayer.

## V. CONCLUSIONS

The electron stimulated decomposition of the organometallic gold precursor, $Au^{III}(acac)Me_2$, adsorbed onto solid substrates produces a film composed of metallic gold atoms embedded in an organic matrix, accompanied by the formation of methane, carbon monoxide, hydrogen, and ethane. Experimental results suggest that carbon atoms removed as $CH_4$ or $C_2H_6$ from the $Au^{III}(acac)Me_2$ precursor during FEBIP were initially associated with the $Au-CH_3$ groups, while electron induced decomposition of the acac ligand can lead to the evolution of carbon monoxide. Based on the electron stimulated reduction kinetics of parent $Au^{III}$ atoms, the total reaction cross section of $Au^{III}(acac)Me_{2(ads)}$ at an incident electron energy of 520 eV was determined to lie between $3.0\times10^{-16}$ and $4.0\times10^{-16}$ $cm^2$. Surface reactions and reactions kinetics were independent of the substrate's chemical identity although as a function of incident electron energy, the total reaction cross section displayed a smooth variation with a maximum between 150 and 200 eV. In growth studies performed under conditions more representative of FEBIP, film deposition was shown not to occur uniformly within the electron irradiated area but rather leads to the formation of discrete, isolated structures.

## ACKNOWLEDGMENTS

The authors would like to acknowledge support from the National Science Foundation (Grant No. CHE-0616873). We also acknowledge the use of the surface analysis laboratory at Johns Hopkins University.

[1]A. E. Grigorescu and C. W. Hagen, Nanotechnology **20**, 292001 (2009).
[2]C. W. Hagen, W. F. van Dorp, P. A. Crozier, and P. Kruit, Surf. Sci. **602**, 3212 (2008).
[3]M. Tanaka, M. Shimojo, M. Han, K. Mitsuishi, and K. Furuya, Surf. Interface Anal. **37**, 261 (2005).
[4]V. Scheuer, H. W. P. Koops, and T. Tschudi, Microelectron. Eng. **5**, 423 (1986).
[5]F. Cicoira, K. Leifer, P. Hoffman, I. Utke, B. Dwir, D. Laub, P. A. Buffat, E. Kapon, and P. Doppelt, J. Cryst. Growth **265**, 619 (2004).
[6]M. A. Henderson, R. D. Ramsier, and J. T. Yates, J. Vac. Sci. Technol. A **9**, 1563 (1991).
[7]T. Bret, S. Mauron, I. Utke, and P. Hoffman, Microelectron. Eng. **78-79**, 300 (2005).
[8]S. H. Kim and G. A. Somorjai, J. Phys. Chem. B **106**, 1386 (2002).
[9]O. Guise, H. Marbach, J. Levy, J. Ahner, and J. T. Yates, Surf. Sci. **571**, 128 (2004).
[10]R. D. Ramsier and J. T. Yates, Surf. Sci. **289**, 39 (1993).
[11]M. A. Henderson, R. D. Ramsier, and J. T. Yates, Surf. Sci. **259**, 173 (1991).
[12]R. D. Ramsier, M. A. Henderson, and J. T. Yates, Surf. Sci. **257**, 9 (1991).
[13]P. A. Crozier, J. Tolle, J. Kouvetakis, and C. Ritter, Appl. Phys. Lett. **84**, 3441 (2004).
[14]I. Utke, A. Luisier, P. Hoffman, D. Laub, and P. A. Buffat, Appl. Phys. Lett. **81**, 3245 (2002).
[15]I. Utke, B. Dwir, K. Leifer, F. Cicoira, P. Doppelt, P. Hoffman, and E. Kapon, Microelectron. Eng. **53**, 261 (2000).
[16]T. Brintlinger, M. S. Fuhrer, J. Melngailis, I. Utke, T. Bret, A. Perentes, P. Hoffman, M. Abourida, and P. Doppelt, J. Vac. Sci. Technol. B **23**, 3174 (2005).
[17]M. Weber, M. Rudolph, J. Kretz, and H. W. P. Koops, J. Vac. Sci. Technol. B **13**, 461 (1995).
[18]J. Kretz, M. Rudolph, M. Weber, and H. W. P. Koops, Microelectron. Eng. **23**, 477 (1994).
[19]K. L. Lee, D. W. Abraham, F. Secord, and L. Landstein, J. Vac. Sci. Technol. B **9**, 3562 (1991).
[20]H. W. P. Koops, J. Kretz, M. Rudolph, and M. Weber, J. Vac. Sci. Technol. B **11**, 2386 (1993).
[21]G. C. Gazzadi and S. Frabboni, J. Vac. Sci. Technol. B **23**, L1 (2005).
[22]P. Bøggild, T. M. Hansen, O. Kuhn, and F. Grey, Rev. Sci. Instrum. **71**, 2781 (2000).
[23]H. W. P. Koops, O. E. Hoinkis, M. E. W. Honsberg, R. Schmidt, R. Blum, G. Bottger, A. Kuligk, C. Liguda, and M. Eich, Microelectron. Eng. **57-58**, 995 (2001).
[24]K. I. Schiffmann, Nanotechnology **4**, 163 (1993).
[25]C. Schoessler and H. W. P. Koops, J. Vac. Sci. Technol. B **16**, 862 (1998).
[26]S. Graells, R. Alcubilla, G. Badenes, and R. Quidant, Appl. Phys. Lett. **91**, 121112 (2007).
[27]K. L. Lee and M. Hatzakis, J. Vac. Sci. Technol. B **7**, 1941 (1989).
[28]A. Botman, J. J. L. Mulders, R. Weemaes, and S. Mentink, Nanotechnology **17**, 3779 (2006).
[29]M. Weber, H. W. P. Koops, M. Rudolph, J. Kretz, and G. Schmidt, J. Vac. Sci. Technol. B **13**, 1364 (1995).
[30]K. Mølhave, D. N. Madsen, A. M. Rasmussen, A. Carlsson, C. C. Appel, M. Brorson, C. J. H. Jacobsen, and P. Boggild, Nano Lett. **3**, 1499 (2003).
[31]I. Utke, P. Hoffman, and J. Melngailis, J. Vac. Sci. Technol. B **26**, 1197 (2008).
[32]H. W. P. Koops, A. Kaya, and M. Weber, J. Vac. Sci. Technol. B **13**, 2400 (1995).
[33]R. M. Langford, T.-X. Wang, and D. Ozkaya, Microelectron. Eng. **84**, 784 (2007).
[34]T. Bret, I. Utke, A. Bachmann, and P. Hoffman, Appl. Phys. Lett. **83**, 4005 (2003).
[35]I. Utke, P. Hoffman, B. Dwir, K. Leifer, E. Kapon, and P. Doppelt, J. Vac. Sci. Technol. B **18**, 3168 (2000).
[36]A. Botman, D. A. M. de Winter, and J. J. L. Mulders, J. Vac. Sci. Technol. B **26**, 2460 (2008).
[37]W. F. van Dorp and C. W. Hagen, J. Appl. Phys. **104**, 081301 (2008).
[38]S. Frabboni, G. C. Gazzadi, and A. Spessot, Physica E (Amsterdam) **37**, 265 (2007).
[39]J. D. Wnuk, J. M. Gorham, S. G. Rosenberg, W. F. van Dorp, T. E. Madey, C. W. Hagen, and D. H. Fairbrother, J. Phys. Chem. C **113**, 2487 (2009).
[40]W. F. van Dorp, J. D. Wnuk, J. M. Gorham, T. E. Madey, D. H. Fairbrother, and C. W. Hagen, J. Appl. Phys. **106**, 074903 (2009).
[41]A. J. Wagner, G. M. Wolfe, and D. H. Fairbrother, J. Chem. Phys. **120**, 3799 (2004).
[42]J. Gorham, J. Torres, G. Wolfe, A. d'Agostino, and D. H. Fairbrother, J. Phys. Chem. B **109**, 20379 (2005).
[43]P. A. Thiel and T. E. Madey, Surf. Sci. Rep. **7**, 211 (1987).
[44]S. Tanuma, C. J. Powell, and D. R. Penn, Surf. Interface Anal. **17**, 911 (1991).
[45]S. Shibata, K. Iijima, and T. H. Baum, J. Chem. Soc. Dalton Trans. **1990**, 1519.
[46]J. F. Moulder, W. F. Stickle, P. E. Sobol, and K. D. Bomben, *Handbook of X-ray Photoelectron Spectroscopy* (Physical Electronics, Chanhassen, 1995).

[47]See supplementary material at http://dx.doi.org/10.1063/1.3295918 for XP spectra illustrating the effect of prolonged x-ray irradiation on dimethyl-(acetylacetonate) gold(III) adsorbed onto silver and an amorphous carbon (a:C) substrates (≈160 K); Faraday cup measurements used to characterize the spatial distribution of electrons generated by the broad beam electron source; and Auger spectra obtained from two locations on the same HOPG substrate exposed to $\approx 1.0 \times 10^{-7}$ Torr of $Au^{III}(acac)Me_2$.
[48]H. Ohashi, H. Ezoe, Y. Okaue, Y. Kobayashi, S. Matsuo, T. Kurisaki, A. Miyazaki, H. Wakita, and T. Yokoyama, Anal. Sci. **21**, 789 (2005).
[49]K. Kishi and S. Ikeda, Appl. Surf. Sci. **5**, 37 (1980).
[50]V. I. Kodolov, I. N. Shabanova, S. N. Babushkina, E. I. Chirkova, and N. V. Keller, J. Struct. Chem. **39**, 912 (1998).
[51]M. G. Miles, G. E. Glass, and R. S. Tobias, J. Am. Chem. Soc. **88**, 5738 (1966).
[52]C. G. MacDonald and J. S. Shannon, Aust. J. Chem. **19**, 1545 (1966).
[53]H. L. Nigg and R. I. Masel, J. Vac. Sci. Technol. A **16**, 2581 (1998).
[54]R. L. Graham, C. D. Bain, H. A. Biebuyck, P. E. Laibinis, and G. M. Whitesides, J. Phys. Chem. **97**, 9456 (1993).